

Article

Characterizing the Synoptic-Scale Precursors of Extreme Precipitation Events in the Southeastern Edge of the Tibetan Plateau: Anomalous Evolution of Atmospheric Dynamic-Thermal Structure

Longguang Chen, Bin Chen *, Ruiyu Zhao * and Xiangde Xu

State Key Laboratory of Severe Weather, Chinese Academy of Meteorological Sciences, Beijing 100081, China

* Correspondence: chenbin@cma.gov.cn (B.C.); ruiyu2016@foxmail.com (R.Z.)

Abstract: Extreme precipitation events frequently occur at the southeastern edge of the Tibetan Plateau (SETP), causing severe disasters. In this study, we selected the top 100 regional extreme precipitation events over the SETP region during the period of 2001–2020, and analyzed their evolutionary characteristics of large-scale thermodynamic anomalies prior to the extreme precipitation events occurring, with the aim of exploring their precursor signals. The results show that, accompanying the wave train propagating across the Eurasian continent and reaching East Asia, the extreme events over SETP during the summer season are dominated by the background large-scale atmospheric circulations characterized by the strengthened Southern Asia high (SAH), the westward-extended Western Pacific subtropical high (WPSH), and an intensified eastern Asia trough. Additionally, an analogue of low-level vortex embedded in the background large-scale circulations is developed at least 4 days prior to the occurrence of extreme events. Under the combined effects of these anomalies, the warm and cold air converge in the SETP area. Further analysis also suggests that the upper-troposphere divergence aloft combined with lower pressures at surface level lead to the upward vertical motion of circulations, along with the enhanced water-vapor transport conveyed both by the East Asian summer monsoon and the Indian summer monsoon. All anomalies mentioned above provide the favorable environment for the occurrence of precipitation extremes in the SETP region.



Citation: Chen, L.; Chen, B.; Zhao, R.; Xu, X. Characterizing the Synoptic-Scale Precursors of Extreme Precipitation Events in the Southeastern Edge of the Tibetan Plateau: Anomalous Evolution of Atmospheric Dynamic-Thermal Structure. *Water* **2023**, *15*, 1407.
<https://doi.org/10.3390/w15071407>

Academic Editor: Paul Kucera

Received: 8 February 2023

Revised: 9 March 2023

Accepted: 1 April 2023

Published: 4 April 2023



Copyright: © 2023 by the authors. Licensee MDPI, Basel, Switzerland. This article is an open access article distributed under the terms and conditions of the Creative Commons Attribution (CC BY) license (<https://creativecommons.org/licenses/by/4.0/>).

1. Introduction

The southeastern edge of the Tibetan Plateau (SETP) is the transition zone from the plateau to the Sichuan Basin, with a highly complex topography and large altitude differences; its maximum altitude difference can reach about half of the troposphere height within a few hundred kilometers. Affected by weather systems at different scales, the spatial distribution of regional precipitation characteristics varies in the SETP. As the population in this area is dense for the whole plateau, the occurrence, development, and formation mechanisms of extreme precipitation in this region deserve more attention. In particular, under the context of global warming, the storms causing extreme precipitation in mid-latitude regions will be stronger, and their impact range will be more extensive [1]. Previous studies revealed that the rainfall of extreme precipitation in the central and eastern Tibetan Plateau (TP) shows an increasing trend [2]. The TP, as a sensitive area in response to climate change, has a maximum center of rainfall located on the SETP [3]. Therefore, the extreme precipitation on the SETP is more obviously affected by climate change.

The rainy season in the Hengduan Mountains on the SETP and the adjacent areas of the Sichuan Basin is from May to September, with 80% of the annual average precipitation [4,5]. Previous studies indicated that the large-scale weather systems affecting extreme precipitation in the SETP are complex, mainly including the South Asian high in upper layers, the

western Pacific subtropical high (WPSH) and short-wave troughs near the TP in middle layers, and the southwest vortex in lower layers [6]. For mesoscale weather systems, the plateau vortex and the southwest vortex have a direct impact on the extreme precipitation in the SETP, and these mesoscale vortices also interact with the large-scale circulation background field, thereby affecting extreme precipitation in different regions [7–9]. On the convective scale, the convection characteristics of precipitation over the TP and SETP are different from those in the other areas of China; there are also great spatial differences in the convective precipitation characteristics within the TP and the summer convective precipitation on the plateau is affected by various factors such as topography [10–12]. Under the joint influence of weather systems at different scales, there are complex energy transfers in the mesoscale systems in the TP region and the Sichuan Basin [13–15]. In addition to complex weather systems, water vapor transport is a key factor in extreme precipitation. For the precipitation in the southeastern TP, the water vapor transport is affected by a combination of the Indian summer monsoon and the East Asian summer monsoon, displaying remarkable multi-scale temporal variability [16].

In view of the complexity of weather systems and terrain, limited observation conditions, and the lack of meteorological observations in the SETP, the mechanisms of extreme precipitation generation and development in this area still need to be determined. In addition, most of the previous studies focused on the extreme precipitation in the Sichuan Basin [17], and few investigated the extreme precipitation in the SETP. Here, we examine the extreme precipitation in the SETP by analyzing large-scale circulation characteristics during extreme precipitation. Moreover, we particularly focus on the variations of atmospheric circulations and thermodynamic anomalies before extreme precipitation. This study aims to reveal the precursor signals of extreme precipitation in terms of large-scale circulations to provide references for understanding the physical mechanisms underpinning extreme precipitation.

The remainder of this paper is organized as follows. Section 2 introduces the data and methods used in this research. Section 3 shows the results, including the precipitation characteristics in the SETP and the characteristics of atmospheric circulation pattern, temperature, and humidity during and before the regional extreme precipitation. The main conclusions and discussion are presented in Section 4.

2. Data and Methods

2.1. Data

The precipitation data used in this study are from two datasets, one of which is the Daily Dataset of Basic Meteorological Elements for China National Surface Weather Stations (version 3.0). This dataset spans from 1981 to 2020 and is released by the National Meteorological Information Center of the China Meteorological Administration, which has been processed by quality control. The other dataset that provided the daily precipitation data is a set of satellite data, i.e., the Integrated Multi-Satellite Retrievals for the Global Precipitation Measurement (GPM) with Gauge Calibration (IMERG-Cal), with a resolution of $0.1^\circ \times 0.1^\circ$. Research has demonstrated that the IMERG-Cal data perform better in evaluating extreme precipitation in Southwest China compared with the ground-based station observations and various satellite datasets [5]. The IMERG-Cal dataset can compensate for the lack in observations caused by the uneven and sparse distribution of weather stations in the SETP (Figure 1a). Because the IMERG data are relatively new, this study focuses on the period of 2001–2020 for which the IMERG data are complete.

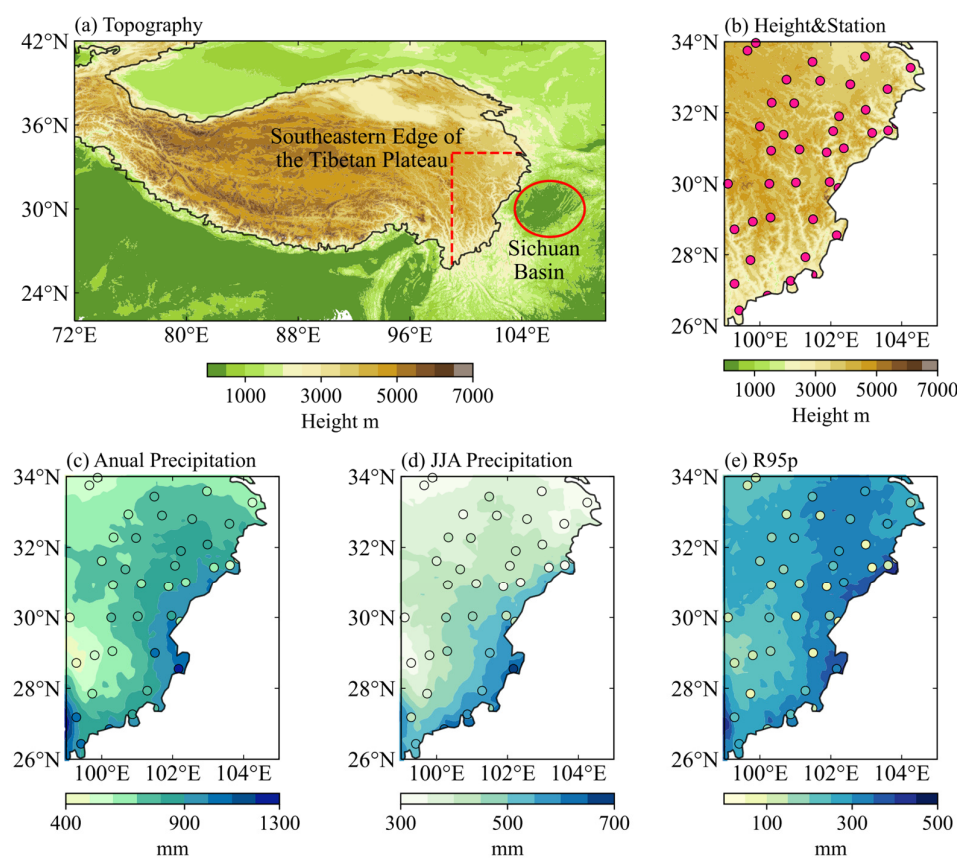


Figure 1. The spatial distributions of the (a) topography, (b) topography of target region with the distribution of the observation stations, (c) annual average precipitation, (d) June–August average precipitation, and (e) annual average extreme precipitation (the total rainfall amount above the 95th percentile on the southeastern edge of the Tibetan Plateau. Unit is in mm day^{-1} in (c–e)). The circle in (a) roughly indicates the area of the Sichuan Basin.

Moreover, the fifth-generation European Center for Medium-Range Weather Forecasts reanalysis (ERA5) dataset is used for the diagnosis of physical quantities, such as atmospheric circulations, wind and water vapor flux, with spatio-temporal resolutions of $0.25^\circ \times 0.25^\circ$ and one hour.

2.2. Methods

2.2.1. Selection of Regional Extreme Precipitation Events

Previous studies have applied different classification criteria for regional extreme precipitation according to the climate characteristics of precipitation in the study area. In this research, the regional extreme precipitation events were identified by combining the climatic characteristics of regional precipitation and the precipitation indicators of rainstorms, and the detailed steps were as follows. Firstly, although previous studies have indicated that the SETP is the precipitation center of the entire plateau, the actual precipitation maximum center appears in the Sichuan Basin due to the terrain of the eastern slope of the plateau. Therefore, in order to better investigate the extreme precipitation characteristics on the SETP, this study focused on the extreme precipitation in the Sichuan Basin adjacent to the southeastern boundary of the TP, i.e., the irregular area surrounded by $99^\circ \text{ E}-105^\circ \text{ E}$, $26^\circ \text{ N}-34^\circ \text{ N}$, and the southeastern boundary of the TP (Figure 1), rather than the precipitation within the Sichuan Basin. Then, the events with the top 100 events on the SETP adjacent to the Sichuan Basin were selected in terms of the largest average rainfall. That is, the IMERG-Cal precipitation grid data from 2001 to 2020 were used to calculate the daily average rainfall in the area, and 100 events with the largest daily rainfall

amount were selected as study objects. Table 1 shows the information on these extreme precipitation events, such as the occurrence time and regional total rainfall amount.

Table 1. Top 100 precipitation events with the largest regional average rainfall in the southeastern edge of the Tibetan Plateau from 2001 to 2020.

Date	Area-Ave-Pre (mm)	Date	Area-Ave-Pre (mm)	Date	Area-Ave-Pre (mm)
2 August 2018	20.45	8 July 2005	14.45	22 June 2003	13.33
19 July 2003	20.38	24 June 2019	14.45	19 June 2014	13.26
22 June 2011	19.79	16 August 2002	14.44	17 July 2020	13.24
28 June 2014	19.54	21 August 2010	14.43	9 July 2005	13.22
16 August 2015	18.83	9 July 2020	14.39	25 July 2020	13.19
16 August 2020	18.14	19 June 2009	14.35	3 August 2009	13.11
29 June 2015	17.76	25 June 2009	14.34	7 July 2004	13.11
6 July 2017	17.74	18 July 2013	14.33	27 July 2012	13.08
22 July 2019	17.7	30 August 2002	14.29	2 July 2017	12.96
29 June 2018	17.68	19 July 2007	14.21	28 July 2018	12.96
10 August 2002	17.56	20 June 2013	14.19	13 June 2020	12.85
17 August 2020	17.49	21 June 2009	14.11	17 August 2015	12.83
29 June 2020	17.47	30 June 2004	14.08	18 August 2020	12.76
11 June 2002	17.39	21 July 2016	14.05	29 June 2002	12.73
21 June 2003	17.27	6 June 2002	13.98	8 August 2015	12.65
30 August 2020	17.19	29 June 2012	13.98	30 June 2020	12.62
14 July 2014	16.99	11 August 2001	13.98	8 July 2019	12.58
18 July 2019	16.93	17 July 2010	13.97	29 June 2016	12.52
14 July 2015	16.34	4 July 2016	13.93	8 August 2017	12.52
6 July 2006	16.27	20 August 2002	13.84	21 June 2018	12.5
8 August 2003	16.27	7 June 2006	13.81	4 July 2002	12.41
21 July 2012	15.88	15 July 2012	13.8	8 July 2004	12.38
9 June 2002	15.82	9 August 2001	13.77	28 June 2010	12.36
30 June 2008	15.64	10 August 2007	13.73	10 June 2008	12.32
18 August 2015	15.51	24 August 2015	13.73	28 July 2019	12.29
10 August 2018	15.38	5 July 2016	13.72	17 July 2007	12.28
7 August 2017	15.36	23 June 2017	13.65	9 August 2014	12.27
17 August 2014	15.14	29 June 2009	13.65	17 July 2016	12.25
28 June 2009	15.14	4 July 2013	13.65	22 July 2012	12.25
3 August 2015	15.11	28 August 2013	13.43	3 July 2012	12.14
30 July 2009	14.91	7 August 2013	13.43	31 July 2009	12.13
3 July 2008	14.76	11 August 2014	13.4	17 June 2020	12.1
4 July 2004	14.58	29 June 2017	13.4		
6 July 2014	14.47	9 July 2010	13.34		

2.2.2. Composite Analysis of Regional Extreme Precipitation Events

After the extreme events were identified, a composite analysis was carried out to obtain the main characteristics of regional extreme precipitation. Although some unique information of single extreme events could be filtered out by composite analysis, the most prominent features of circulations for precipitation were retained in the results. In addition, the composite circulation anomalies were analyzed to investigate the characteristics of regional extreme precipitation different from the climate state. In several previous studies, the study period of the climate state on the SETP was the rainy season, namely May–September [9]. However, to characterize the characteristics of atmospheric conditions on the days of extreme precipitation events and on 8 days before them in summer (June to August), the average from June to August was used to analyze the climate state in this study.

2.2.3. Analysis Method for Wave Action Flux

Wave action flux can represent the horizontal momentum transport in wave train activity. Takaya and Nakamura [18] obtained a tool to better diagnose the small-amplitude

disturbance superimposed on basic flow based on Eliassen–Palm flux, and the expression is as follows:

$$W = \frac{p \cos \phi}{2|U|} \left(\begin{array}{l} \frac{U}{a^2 \cos^2 \phi} \left[\left(\frac{\partial \psi'}{\partial \lambda} \right)^2 - \psi' \frac{\partial^2 \psi'}{\partial \lambda^2} \right] + \frac{V}{a^2 \cos \phi} \left[\frac{\partial \psi'}{\partial \lambda} \frac{\partial \psi'}{\partial \phi} - \psi' \frac{\partial^2 \psi'}{\partial \lambda \partial \phi} \right] \\ \frac{U}{a^2 \cos \phi} \left[\frac{\partial \psi'}{\partial \lambda} \frac{\partial \psi'}{\partial \phi} - \psi' \frac{\partial^2 \psi'}{\partial \lambda \partial \phi} \right] + \frac{V}{a^2} \left[\left(\frac{\partial \psi'}{\partial \phi} \right)^2 - \psi' \frac{\partial^2 \psi'}{\partial \phi^2} \right] \\ \frac{f_0^2}{N^2} \left\{ \frac{U}{a \cos \phi} \left[\frac{\partial \psi'}{\partial \lambda} \frac{\partial \psi'}{\partial z} - \psi' \frac{\partial^2 \psi'}{\partial \lambda \partial z} \right] + \frac{V}{a} \left[\frac{\partial \psi'}{\partial \phi} \frac{\partial \psi'}{\partial z} - \psi' \frac{\partial^2 \psi'}{\partial \phi \partial z} \right] \right\} \end{array} \right) \quad (1)$$

where ψ' represents the stream function; λ the longitudes; Φ the latitudes; U the basic flow; and p the normalized atmospheric pressure. In this research, Takaya–Nakamura flux was used to analyze the extreme precipitation events after the classification and composite process and diagnosed the formation process of their circulations.

2.2.4. Water Vapor Flux and Its Divergence

The zonal water vapor flux (Q_u), meridional water vapor flux (Q_v), and water vapor flux divergence (Q_{div}) from the surface (p_s) to 300 hPa can be expressed as follows:

$$Q_u(x, y, t) = \frac{1}{g} \int_{300}^{p_s} q(x, y, p, t) u(x, y, p, t) dp \quad (2)$$

$$Q_v(x, y, t) = \frac{1}{g} \int_{300}^{p_s} q(x, y, p, t) v(x, y, p, t) dp \quad (3)$$

$$Q_{\text{div}} = \frac{1}{g} \int_{300}^{p_s} \nabla \cdot (V q) dp \quad (4)$$

where q denotes the specific humidity; p the pressure; u the zonal wind speed; and v the meridional wind speed.

3. Results

3.1. Precipitation Characteristics on the Southeastern Edge of the Tibetan Plateau

The overall precipitation characteristics are investigated by statistics for rainfall amount at the junction between the SETP and the Sichuan Basin during 2001–2020. Figure 1 shows spatial distributions of the topography, observation stations, annual average precipitation, and summer average precipitation in the SETP. In addition, the distributions of the annual average rainfall amount of extreme precipitation events (the total rainfall amount above the 95th percentile) and precipitation days with rainfall amount $\geq 50 \text{ mm day}^{-1}$ are presented. The results indicate that the IMERG data show relative agreement with the station observations in terms of spatial distribution (Figure not shown). However, compared with the observations, the total rainfall amount and extreme value of the GPM precipitation are lower, while the rainfall amount at the 95th percentile and the heavy precipitation days ($\geq 50 \text{ mm day}^{-1}$) for the IMERG data are larger, indicating noticeable spatial differences in precipitation in the SETP. The spatial distributions of the annual rainfall, rainy season precipitation, extreme rainfall, and days with rainfall amount $\geq 50 \text{ mm day}^{-1}$ (Figure 1b–e) suggest that the common large-value area of these four variables is located at the junction between the SETP and the Sichuan Basin, with the maximum center around the point of 102° E, 28° N at the southeastern edge of the TP (Figure 1b–e). For the 100 extreme precipitation events in the study area, the regional average rainfall amount is greater than 12 mm day^{-1} , with a maximum of $20.45 \text{ mm day}^{-1}$, and the rainfall intensity variability is relatively uniform. However, it should be noted that there are large differences in the spatial distribution of rainfall amounts in the study area.

3.2. Atmospheric Circulation Pattern and Temperature and Humidity Characteristics during Regional Extreme Precipitation

The circulation associated with regional extreme precipitation is featured by a synergistic configuration of the South Asian high, upper-level jets, WPSH, and the southwest vortex, as shown in Figure 2. At the upper level (200 hPa), the southern TP and the precipitation area are controlled by the center of the South Asian high (Figure 2d). Thus, there is strong divergence at the upper level, and the southerly airflow prevails at the upper level over the precipitation area and its adjacent areas (Figure 2a). Additionally, upper-level jets appear in the northern TP. At the middle level (500 hPa), the wind field on the western side of the WPSH in the Sichuan Basin and its adjacent areas shows the cyclonic characteristic (Figure 2e). Combined with the vertical profile, positive vorticity can be found at the middle level, corresponding to the location of the vortex center. At the low level (850 hPa), the closed contour lines and the cyclonic wind field are more clearly visible in the Sichuan Basin and its adjacent areas on the eastern side of the SETP (Figure 2f), indicating the presence of the southwest vortex at the low level.

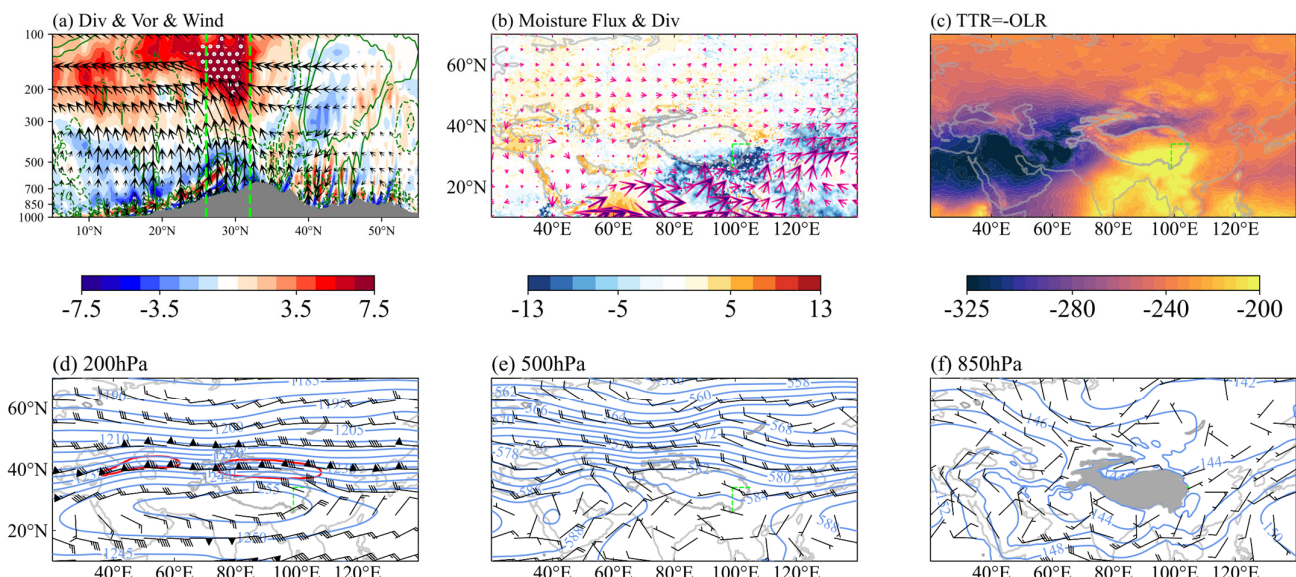


Figure 2. (a) Vertical motion ω (arrows), divergence (colored areas), and vorticity (grey areas) averaged in 26° N– 34° N, (b) water vapor flux (pink arrows) and water vapor flux divergence (colored areas; $10^{-5} \text{ kg m}^{-2} \text{ s}^{-1}$), (c) top net thermal radiation (W m^{-2}), and (d–f) horizontal wind (barbs) and geopotential height fields (black lines) at (d) 200 hPa, (e) 500 hPa, and (f) 850 hPa. The area within green dashed lines denotes target region of this study. The red lines in (d) represent the upper-level jet zones with the wind speed $\geq 30 \text{ m s}^{-1}$ on the extreme precipitation day. The terrain is masked as the gray shading in figure (a) (corresponding to right coordinate).

The analysis of water vapor flux indicates that the whole-layer water vapor convergence is strong over the southern TP and the area south of it. The region with the strongest water vapor convergence is located in the area from the SETP to the Sichuan Basin. The distribution of the water vapor flux from the tropical ocean to the vicinity of 30° N shows a southwest–northeast pattern. In particular, intense water-vapor transport flux appears in the area from the Bay of Bengal to the SETP. This result is explained by the fact that the wind field in this region is dominated by the southwesterly flow, which provides favorable conditions for the water vapor transport responsible for extreme precipitation.

In terms of vertical velocity, the strong ascending flow appears in the extreme precipitation area (Figure 2a). There is noticeable wind convergence at the low level on the north and south sides of the precipitation area, while an apparent large-value area of top net thermal radiation appears on the southern side of the upper-level strong divergence area. The top net thermal radiation can represent the absorption of atmospheric long-wave

radiation by clouds in the area, especially the development of convective clouds near low-latitude areas. Under the background of the above circulation configuration and water vapor transport conditions, the large-value area of the top net thermal radiation is located in the southern TP, the area south of it, and the surrounding areas of the Sichuan Basin, suggesting that the absorption capacity of clouds for atmospheric long-wave radiation in these areas is considerably stronger than in other areas. With the development of the strong convection mentioned above, it can be seen that the development of convective clouds in this area is vigorous, and the convective activities are strong.

3.3. Evolution Characteristics of Synoptic-Scale Circulations and Temperature and Humidity Anomalies before Regional Extreme Precipitation

The composite analysis of 100 extreme precipitation events is conducted in this section. Since the time scale of the evolution of synoptic-scale circulations is 8–10 days, the evolutions of the circulation pattern and thermodynamic anomalies for 8 days before regional extreme precipitation is analyzed to preliminarily reveal the obvious signals that characterize the occurrence and development of precipitation processes.

3.3.1. Anomalies of Synoptic-Scale Atmospheric Circulations and Geopotential Height

Figure 3 presents the distribution of these variables on the 8th day and 4th day before extreme precipitation and on the day of extreme precipitation. The results suggest that there are obvious circulation variations near the center of South Asian high at the upper level (200 hPa). A zone of negative geopotential height anomaly across the Eurasian continent appears in the jet area near 40° N on the northern side of the South Asian high. With the imminent occurrence of extreme precipitation, the geopotential height anomaly gradually turns from negative to positive, and the main range of the northern Eurasian continent is controlled by the positive geopotential height anomaly. In addition, the positive anomaly center appears in the Siberian region, and the South Asian high center gradually strengthens. The eastern part of the South Asian high center directly controls the precipitation area, and the upper-level divergence intensifies in the precipitation area, conducive to the development of strong convection. At the middle level (500 hPa), the variation in the geopotential height anomaly on the TP and its adjacent areas is noticeable. Specifically, on the 8th day before extreme precipitation, there are obvious negative geopotential height anomalies on the central TP, which are not significant on the whole plateau. The northern, western, and southern TP regions are controlled by a positive geopotential height anomaly, while the eastern TP is controlled by a negative anomaly. On the 4th day before extreme precipitation, the eastern TP is controlled by a weak positive geopotential height anomaly, while a negative geopotential height anomaly appears on the northwestern side of the TP. On the day of extreme precipitation, the TP and its adjacent areas are controlled by a positive geopotential height anomaly. There is an area with an obvious positive geopotential height anomaly on the northwestern side of the TP, whose center is located north of the TP. With the strengthening of the positive anomaly, the troughs in the southwestern and southeastern TP strengthen, and the mesocyclone in the precipitation area enhances, which favors the development of strong convection. Meanwhile, the positive geopotential height anomaly near the WPSH center continues to strengthen, and the stable southwesterly airflow on the western side of the WPSH is conducive to the maintenance of water vapor transport at the middle and lower levels. At the low level (850 hPa), the variation in the geopotential height anomaly on the TP and its adjacent areas is also noticeable. This area is first controlled by a negative geopotential height anomaly. As the negative anomaly gradually strengthens, the negative anomaly area is divided into the northwestern and southeastern parts. The negative anomaly in the southeastern part strengthens near the Sichuan Basin, and the cyclonic circulation is considerably enhanced, characterizing to a certain extent the development of the low-level southwest vortex associated with extreme precipitation. Overall, the geopotential height anomaly during extreme precipitation is

mainly characterized by strengthening in the upper level and weakening in the lower level, which are favorable for the enhancement in convection activities.

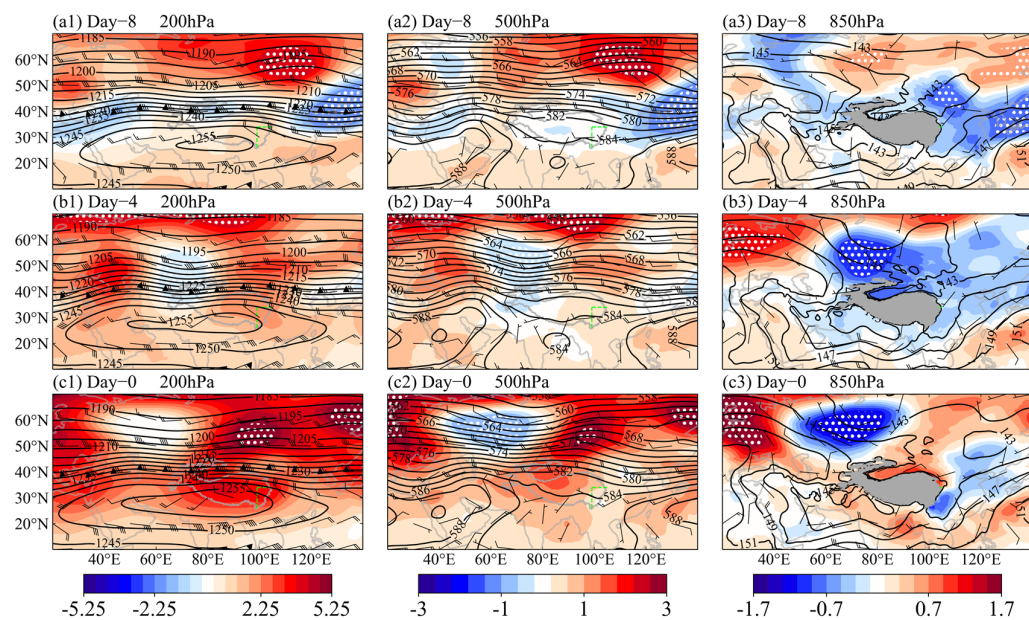


Figure 3. Composite wind field (black barbs), geopotential height field (black contours; dapgm), and geopotential height anomalies (colored areas; dapgm) on the (a1–a3) 8th day and (b1–b3) 4th day before the extreme precipitation and (c1–c3) on the day of the extreme precipitation at 200 hPa (left column), 500 hPa (middle column), and 850 hPa (right column). The dotted areas indicate that the anomalies are statistically significant at the 95% confidence level.

With the atmospheric circulation anomalies mentioned above, the variation in whole-layer water vapor transport is also significant (Figure 4). In terms of the direction and source of water vapor transport, on the 8th day before the precipitation, the water vapor transport in the precipitation area shows a zonal pattern, mainly from the Indian Ocean in the southwest. The water vapor from the South China Sea can be ignored. However, the zonal water vapor transport to the east weakens with time, while the meridional water vapor transport to the north strengthens. Especially during the precipitation period, the zonal water vapor transport is the strongest, the water vapor from the tropical western Pacific increases, and there is water vapor transported meridionally from the back of the TP to the south. Moreover, before the precipitation, it is evident that the negative values of water-vapor flux divergence increase significantly in the precipitation area and on the southern side of the TP, indicating the strong water vapor convergence in these regions, especially on the southern side of the TP towards the extreme precipitation day. The water vapor from the Indian Ocean, the tropical western Pacific, and the northern side of the TP strengthens and converges at the SETP, forming cyclonic convergence, which is conducive to the development of extreme precipitation.

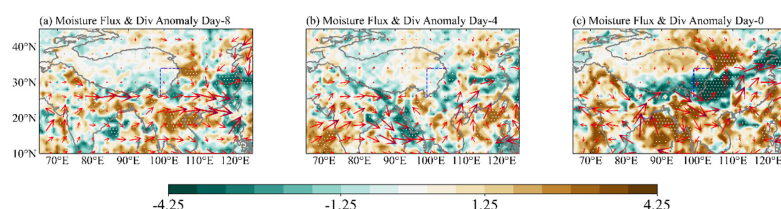


Figure 4. Anomalies ($10^{-5} \text{ kg m}^{-2} \text{ s}^{-1}$) of the water vapor flux (black arrows) and divergence (colored areas) on the (a) 8th day and (b) 4th day before the extreme precipitation and (c) on the day of the extreme precipitation. The dotted areas indicate the anomalies passing the significance test at the 95% confidence level.

3.3.2. Wave Action Flux Anomaly before Regional Extreme Precipitation

Before the extreme precipitation, the wave action flux (Figure 5) obviously develops along the direction of alternating positive and negative geopotential height anomalies. In addition to the geopotential height anomaly center, strong wave action-flux also appears near the upper-level jet zones, which is related to the momentum transport near jet zones. However, as the geopotential height anomaly at the upper level over the Eurasian continent is gradually dominated by the positive anomaly, the entire TP becomes a region of wave action-flux convergence, especially the SETP. This result demonstrates that energy transport in the SETP is relatively intense, which may be related to the kinetic energy transport for extreme precipitation. Eight days before the extreme precipitation, the upper-level jet zone is relatively stable in the northern TP, which is conducive to the continuous kinetic-energy transport to the plateau and thus supports the development of strong convection.

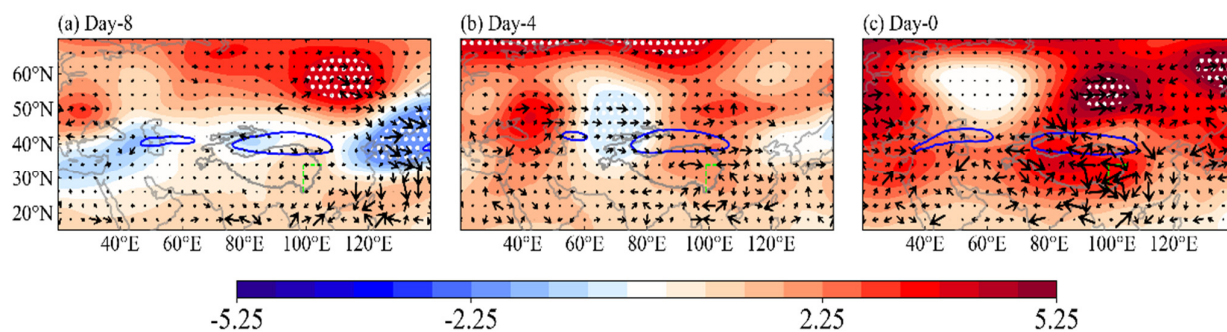


Figure 5. Wave action flux (black arrows) and geopotential height anomaly (colored areas; dagpm) at 200 hPa on the (a) 8th day and (b) 4th day before the extreme precipitation and (c) on the day of the extreme precipitation. The blue line represents the upper-level jet zone with the wind speed up to 30 m s^{-1} , and the dotted area denotes the values passing the significance test at the 95% confidence level.

3.3.3. Atmospheric Temperature and Humidity Structure and Convective Activity Anomaly

Figure 6 shows the vertical profiles of the anomalies of atmospheric temperature, vertical velocity, and geopotential height averaged in 99°E – 105°E on the 8th day and 4th day before the extreme precipitation and on the day of the extreme precipitation. It can be seen that the temperature anomaly presents a dipole pattern of “colder in upper layers and warmer in lower layers”, and the positive temperature anomaly controls in the middle and lower levels below 200 hPa. With 150–200 hPa as the boundary, there is a large temperature gradient between the upper level and middle-lower levels. This dipole pattern of temperature anomaly does not initially appear in the extreme precipitation area but is located north of the precipitation area near 50°N . With the formation of extreme precipitation, the temperature anomaly center and geopotential height anomaly center gradually strengthen and move southward to the precipitation area from the area north of it, and the atmospheric baroclinity near the anomaly center strengthens. This transfer process of temperature anomaly from high latitudes to low latitudes also suggests that the extreme precipitation in the SETP is particularly affected by the anomaly of atmospheric thermodynamic structure in high latitudes. On the day of extreme precipitation, the dipole pattern of temperature anomaly, namely “colder in upper layers and warmer in lower layers”, peaks near 30°N . This atmospheric instability structure eventually results in a vertical circulation situation that favors the formation of extreme precipitation, i.e., descending motion controls the north and south sides and ascending motion controls the precipitation area. This dipole pattern of the temperature anomaly is particularly significant near 50°N , where the intensity of the temperature anomaly is significantly stronger. Eventually, anomalous cold airflow invades from the lower level to the northern side of the precipitation area, resulting in the strengthening of low-level convergence

over the precipitation area and thereby facilitating the development of convection. It is worth noting that such temperature and geopotential anomalies occur together in the vicinity of the upper-level jet zones. Whether the occurrence and development of extreme precipitation is associated with energy transport of jets requires further attention in future studies.

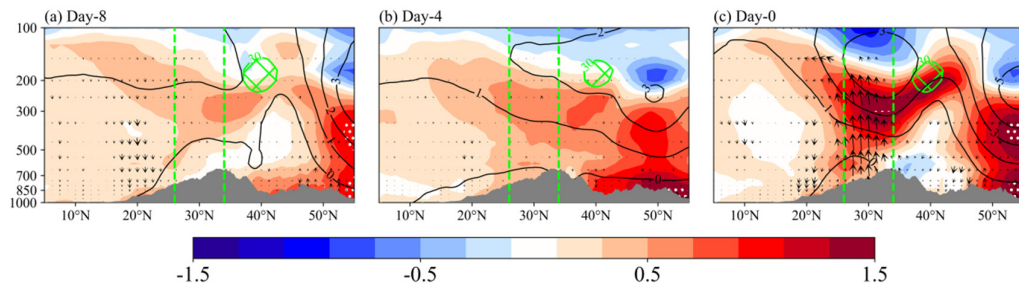


Figure 6. Latitude–altitude cross–section of the anomalies of atmospheric temperature (colored areas; K), vertical velocity (black arrows) and geopotential height (black lines) in 99° E– 105° E on the (a) 8th day and (b) 4th day before the extreme precipitation and (c) on the day of the extreme precipitation. The dotted areas indicate the anomalies exceeding the significance test at the 95% confidence level. The terrain is masked as the gray shading (corresponding to right coordinate).

To further reveal the atmospheric circulation characteristics corresponding to the above temperature anomaly structure, we analyzed the vorticity and divergence associated with extreme precipitation. Figure 7 presents the vertical profiles of the anomalies of atmospheric divergence and vorticity fields. The results suggest that the whole-layer divergence anomaly weakens first and then strengthens, and it enhances significantly when extreme precipitation occurs. In the precipitation area, the positive divergence anomaly persists in the middle and upper levels above 200 hPa on the 8th day before the precipitation, corresponding to the development of the South Asian high. However, at 500 hPa, the negative divergence anomaly persists in the precipitation area, i.e., there is continuous convergence at the low level and thus the ascending motion gradually develops. With the development of the divergence anomaly, the vorticity anomaly is further enhanced. Such a temperature and humidity structure is especially favorable for convective development. As shown in Figure 7c, there is strong divergence at the upper level and convergence at the lower level on the day of precipitation, which coincides with the results in Figure 6c.

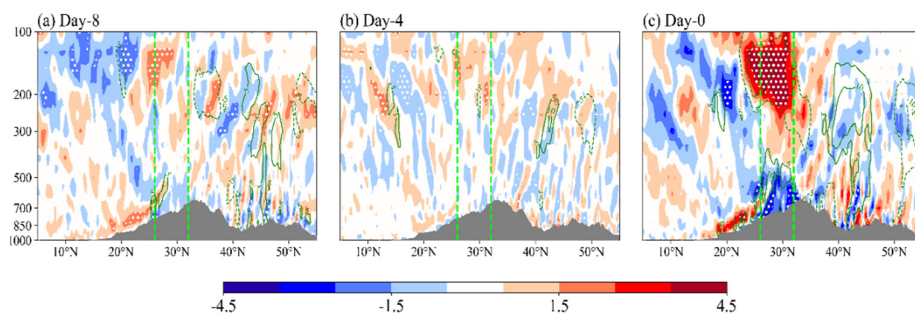


Figure 7. Latitude–altitude vertical cross section of the anomalies of vorticity (green solid lines; 10^{-6} s^{-1}) and divergence (colored areas) in 99° E– 105° E on the (a) 8th day and (b) 4th day before the extreme precipitation and (c) on the day of the extreme precipitation. The dotted areas mean the anomalies passing the significance test at the 95% confidence level, and the unit on the y–axis is hPa.

To investigate the convective activity intensity in the precipitation area, we analyzed the variation characteristics of the top net thermal radiation anomaly for 8 days before the extreme precipitation, as shown in Figure 8. It can be found that the top net thermal radiation in the precipitation area and the surrounding area of the TP generally shows

positive anomalies within 8 days before the extreme precipitation. However, the positive anomalies are not significant for a few days before the precipitation, and the top net thermal radiation increases significantly only for 1–2 days before the precipitation and peaks on the day of the precipitation. This result implies that 2 days before the extreme precipitation, clouds over the precipitation area and its adjacent areas thicken significantly, the development of convective clouds is more vigorous, cloud-top height increases, and the absorption for long-wave radiation obviously increases. In terms of temporal evolution, the variation in convection intensity on the SETP lags behind that in the Sichuan Basin of the eastern part, indicating that there is a certain relationship in the connection between these two regions. The specific mechanism may need further analysis.

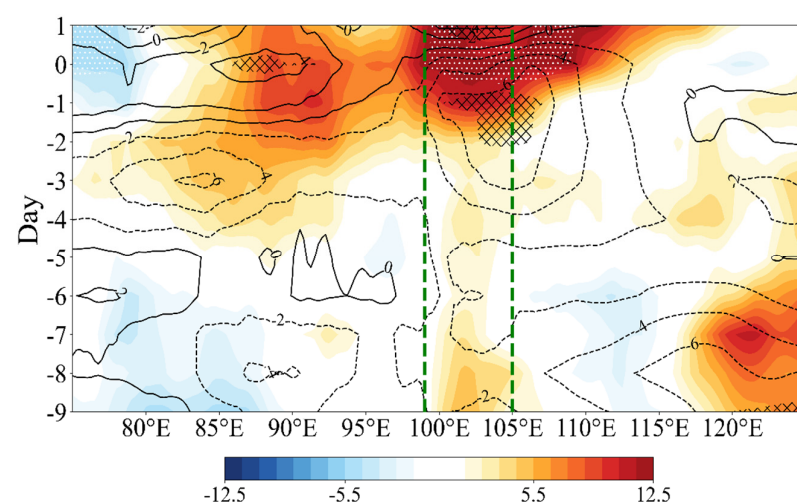


Figure 8. Latitude–altitude cross section of the composite anomalies of vorticity (green solid lines; 10^{-6} s^{-1}) and divergence (colored areas) in 99° E – 105° E . The dotted areas denote the anomalies significance at 95% confidence level.

4. Conclusions and Discussion

4.1. Conclusions

Extreme precipitation events occur frequently in the SETP and cause serious disasters, but few studies have examined their precursors. Based on the station observations, the top net thermal radiation from satellite data, and the ERA5 data, we select 100 extreme precipitation events with the largest average rainfall in the SETP from 2001 to 2020 in this study. Moreover, the evolution characteristics of large-scale thermodynamic structure within 8 days before extreme precipitation are analyzed using synthetic analysis and atmospheric thermodynamic calculation methods. Based on this, an attempt is made to identify the significant precursor signals for the occurrence of extreme precipitation in the SETP. The main conclusions are summarized as follows:

In terms of dynamic characteristics, the upper-level jet on the northern side of the South Asian high continues to be maintained on the northern side of the TP within 8 days before the precipitation, which is favorable for the continuous momentum transport from the upstream to the center of the South Asian high. This situation is not only conducive to the strengthening of the South Asian high, but also beneficial to the enhancement in upper-level divergence over the precipitation area in the eastern South Asian high center, thereby favoring the development of strong convection. At the middle level, the WPSH center is stable from eastern China to the ocean, which is favorable for the water vapor transport by southwesterly airflow on the western side of the WPSH and the middle-level convergence over the precipitation area. At the lower level, the circulations on the northern and southern sides of the TP show relatively pronounced fluctuations. This circulation pattern facilitates the water vapor transport from the Bay of Bengal to the southern side of the TP, forming a superimposed structure of an anticyclonic enhancement and a cyclonic

enhancement on the southern and southeastern sides of the TP. This superimposed structure results in the development of the southwest vortex in the precipitation area, significantly enhancing the convergence of water vapor from the Indian Ocean and western Pacific in the extreme precipitation area. Overall, accompanying the wave train that propagates across the Eurasian continent and reaches East Asia, the extreme events over SETP during the summer season are dominated by the background large-scale atmospheric circulations characterized by the strengthened Southern Asia high (SAH), the westward extended Western Pacific subtropical high (WPSH), and a deepened eastern Asia trough.

For the thermal characteristics, the vertical distribution of temperature anomalies near 50° N in the area north of the precipitation area shows a pattern of “colder in upper layers and warmer in lower layers” for 8 days before the extreme precipitation, and the geopotential height anomaly center is located at the junction of positive and negative temperature anomalies. This temperature anomaly pattern leads to regional atmospheric instability, which is conducive to the development of convection. Further analysis also suggests that the upper-troposphere divergence aloft combined with lower pressures at surface lead to upward vertical motion of circulations, along with the enhanced water vapor transport conveyed both by the East Asian summer monsoon and the Indian summer monsoon, ultimately leading to extreme precipitation. This conclusion related to the convective development is further confirmed by cloud radiation from satellite observations.

4.2. Discussion

Although a great deal of research has been devoted to exploring the factors influencing the occurrence of the heavy rainfall over Southern China, including the SETP region of this study [11,14,15,19–26], few studies have been carried out with a focus on the SETP of this study. However, parts of our results could be compared with those studies. For example, Xu et al. [24] showed that the large-scale circulations responsible for the summer heavy rainfall events over the Sichuan Basin are featured by the configuration of eastward-extended SAH, the westward-extended Western North Pacific Subtropical High, and an obvious low-level vortex, which agree with our results in this study. Zhang et al. [22] also pointed out that the westward extension of Western North Pacific Subtropical High could drive tropical cyclones southward and then increase the occurrence of extreme precipitation in South China. Nie and Sun [9] and Qian et al. [27] stated that the atmospheric wave train propagates almost a week before heavy precipitation over the southwest of China could give rise to an anomalous low over the eastern Tibetan Plateau, which has been reconfirmed by this study. Other studies also emphasized the Tibetan Plateau vortices and southwest vortices [14,15,28,29], and interactions between the Indian–Myanmar trough and the East Asia colder trough, which also been verified by the results of this study.

Previous studies have explored the impacts of tropical cyclones on the formation of extreme rainfall in the southwest of China [22,30]. In this sense, one limitation of our study presented here is that we did not exclude extreme precipitation events that were influenced by tropical cyclones. However, considering the lower amount of tropical cyclones arriving at the SETP region, the main conclusion would possibly not change after removing the impacts of tropical cyclones, which can be explored in a further study. Furthermore, the role of surface SST over the Pacific ocean or North Atlantic in modulating the extreme precipitation has been explored in previous studies [22,23]; however, we did not take account of this factor due to the scope of this study, however, it merits a deeper study.

Overall, the results of this study reveal the main thermodynamic characteristics of extreme precipitation and its evolution in the SETP before its formation. Some precursor signals of extreme precipitation in this area are identified. Some of the precursor signals are strong and can last for 8 days, which are significant features and easily identified. These synoptic-scale thermodynamic anomaly features can provide references for the understanding and prediction of extreme precipitation in the SETP. Meanwhile, the detailed physical mechanisms of these signals, such as the diagnosis and formation mechanisms of water vapor transport related to thermodynamic processes, and the role of other factors

including but not limited to low-level jets, SST, and tropical cyclones, points to the need for future studies.

Author Contributions: Methodology, L.C., B.C. and X.X.; validation, L.C., B.C. and R.Z.; data curation, L.C., B.C. and R.Z.; writing, L.C.; funding acquisition, B.C. and X.X. All authors have read and agreed to the published version of the manuscript.

Funding: This research was funded by the Second Tibetan Plateau Comprehensive Scientific Expedition and Research Program (2019QZKK0105), the S&T Development Fund of CAMS (2021KJ021), and the National Natural Science Foundation of China (Grant No. 91937301).

Data Availability Statement: Not applicable.

Acknowledgments: We thank ECMWF for the ERA-interim data; and thank NASA for the GPM-IMERG precipitation data. The ERA-5 dataset can be obtained from <https://www.ecmwf.int/en/forecasts/datasets/reanalysis-datasets/era5>, accessed on 1 September 2021 and the GPM-IMERG dataset can be obtained from https://disc.gsfc.nasa.gov/datasets/GPM_3IMERGDF_06/summary?keywords=GPM, accessed on 1 May 2022.

Conflicts of Interest: The authors declare no conflict of interest.

References

1. Dai, P.; Nie, J. Robust expansion of extreme midlatitude storms under global warming. *Geophys. Res. Lett.* **2022**, *49*, e2022GL099007. [[CrossRef](#)]
2. You, Q.; Kang, S.; Aguilar, E.; Yan, Y. Changes in daily climate extremes in the eastern and central Tibetan Plateau during 1961–2005. *J. Geophys. Res. Atmos.* **2008**, *113*, 1639–1647. [[CrossRef](#)]
3. Cao, Y.; You, Q.; Ma, Q.; Meng, X. Probability distribution for the summer extreme precipitation in the Qinghai-Tibetan Plateau. *Plateau Meteorol.* **2017**, *36*, 1176–1187. (In Chinese)
4. Dong, D.H.; Huang, G.; Tao, W.C.; Wu, R.G.; Hu, K.M.; Li, C.F. Interannual variation of precipitation over the Hengduan Mountains during rainy season. *Int. J. Climatol.* **2018**, *38*, 2112–2125. [[CrossRef](#)]
5. Nie, Y.; Sun, J. Evaluation of high-resolution precipitation products over southwest China. *J. Hydrometeorol.* **2020**, *21*, 2691–2712. [[CrossRef](#)]
6. Fu, Y.; Ma, Y.; Zhong, L.; Yang, Y.; Guo, X.; Wang, C.; Xu, X.; Yang, K.; Xu, X.; Liu, L.; et al. Land surface processes and summer cloud-precipitation characteristics in the Tibetan Plateau and their effects on downstream weather: A review and perspective. *Natl. Sci. Rev.* **2020**, *7*, 500–515. [[CrossRef](#)]
7. Chen, Y.R.; Li, Y.Q. Convective characteristics and formation conditions in an extreme rainstorm on the eastern edge of the Tibetan Plateau. *Atmosphere* **2021**, *12*, 381. [[CrossRef](#)]
8. Cai, S.; Huang, A.; Zhu, K.; Yang, B.; Yang, X.; Wu, Y.; Mu, X. Diurnal cycle of summer precipitation over the Eastern Tibetan Plateau and surrounding regions simulated in a convection-permitting model. *Clim. Dyn.* **2021**, *57*, 611–632. [[CrossRef](#)]
9. Nie, Y.; Sun, J. Synoptic-scale circulation precursors of extreme precipitation events over southwest China during the rainy season. *J. Geophys. Res. Atmos.* **2021**, *126*, e2021JD035134. [[CrossRef](#)]
10. Fu, S.; Li, W.; Sun, J.; Zhang, J.; Zhang, Y. Universal evolution mechanisms and energy conversion characteristics of long-lived mesoscale vortices over the Sichuan Basin. *Atmos. Sci. Lett.* **2015**, *16*, 127–134. [[CrossRef](#)]
11. Fu, S.M.; Mai, Z.; Sun, J.H.; Li, W.L.; Ding, Y.; Wang, Y.Q. Impacts of convective activity over the Tibetan Plateau on plateau vortex, southwest vortex, and downstream precipitation. *J. Atmos. Sci.* **2019**, *76*, 3803–3830. [[CrossRef](#)]
12. Meng, Y.; Sun, J.; Zhang, Y.; Fu, S. A 10-year climatology of mesoscale convective systems and their synoptic circulations in the Southwest Mountain area of China. *J. Hydrometeorol.* **2021**, *22*, 23–41. [[CrossRef](#)]
13. Li, Y.D.; Wang, Y.; Song, Y.; Hu, L.; Gao, S.T.; Fu, R. Characteristics of summer convective systems initiated over the Tibetan Plateau. Part I: Origin, track, development, and precipitation. *J. Appl. Meteorol. Climatol.* **2008**, *47*, 2679–2695. [[CrossRef](#)]
14. Fu, S.-M.; Sun, J.-H.; Zhao, S.-X.; Li, W.-L. An analysis of the eddy kinetic energy budget of a southwest vortex during heavy rainfall over South China. *Atmos. Ocean. Sci. Lett.* **2009**, *2*, 135–141. [[CrossRef](#)]
15. Fu, S.M.; Sun, J.H.; Zhao, S.X.; Li, W.L. The energy budget of a southwest vortex with heavy rainfall over South China. *Adv. Atmos. Sci.* **2011**, *28*, 709–724. [[CrossRef](#)]
16. Chen, B.; Zhang, W.; Yang, S.; Xu, X.D. Identifying and contrasting the sources of the water vapor reaching the subregions of the Tibetan Plateau during the wet season. *Clim. Dyn.* **2019**, *53*, 6891–6907. [[CrossRef](#)]
17. Qian, C.; Ye, Y.; Zhang, W.; Zhou, T. Heavy rainfall event in mid-august 2020 in Southwestern China: Contribution of anthropogenic forcing and atmospheric circulation. *Bull. Am. Meteorol. Soc.* **2022**, *103*, S111–S117. [[CrossRef](#)]
18. Takaya, K.; Nakamura, H. A formulation of a phase-independent wave-activity flux for stationary and Migratory Quasigeostrophic Eddies on a Zonally varying basic flow. *J. Atmos. Sci.* **2001**, *58*, 608–627. [[CrossRef](#)]
19. Chen, Y.; Shi, Y.; Li, Y.; Wang, C. The study of a kind of circulations characters on sustaining heavy rain in Sichuan Basin. *Plateau Mt. Meteorol. Res.* **2010**, *30*, 29–34. (In Chinese)

20. Zhao, Y.; Wang, H. A case study on plateau vortex inducing southwest vortex and producing extremely heavy rain. *Plateau Meteorol.* **2010**, *029*, 819–831. (In Chinese)
21. Wei, W.; Zhang, R.; Wen, M.; Rong, X.; Li, T. Impact of Indian summer monsoon on the South Asian High and its influence on summer rainfall over China. *Clim. Dyn.* **2014**, *43*, 1257–1269. [[CrossRef](#)]
22. Zhang, Q.; Zheng, Y.; Singh, V.; Luo, M.; Xie, Z. Summer extreme precipitation in eastern China: Mechanisms and impacts. *J. Geophys. Res. Atmos.* **2017**, *122*, 2766–2778. [[CrossRef](#)]
23. Li, G.; Chen, J.; Wang, X.; Luo, X.; Yang, D.; Zhou, W.; Tan, Y.; Yan, H. Remote impact of North Atlantic sea surface temperature on rainfall in southwestern China during boreal spring. *Clim. Dyn.* **2018**, *50*, 541–553. [[CrossRef](#)]
24. Xu, X.; Huang, A.; Huang, D.; Zhang, Y.; Gu, C.; Cai, S.; Tang, Y.; Zhao, Z.; Zeng, J. What are the dominant synoptic patterns leading to the summer regional hourly extreme precipitation events over central-eastern Tibetan Plateau and Sichuan Basin? *Geophys. Res. Lett.* **2023**, *50*, e2022GL102342. [[CrossRef](#)]
25. Yi, S.J.; Zheng, F.; Xiao, T. Comparative analysis of environmental fields of two typical rainstorm cases in southwest China. *Clim. Environ. Res.* **2019**, *24*, 73–115. (In Chinese)
26. Qian, Q.; Wu, R.; Jia, X. Persistence and nonpersistence of East and Southeast Asian rainfall anomaly pattern from spring to summer. *J. Geophys. Res. Atmos.* **2020**, *125*, e2020JD033404. [[CrossRef](#)]
27. Li, L.; Zhang, R.; Wu, P.; Wen, M.; Duan, J. Roles of Tibetan Plateau vortices in the heavy rainfall over southwestern China in early July 2018. *Atmos. Res.* **2020**, *245*, 105059. [[CrossRef](#)]
28. Ni, C.; Li, G.; Xiong, X. Analysis of a vortex precipitation event over Southwest China using AIRS and in situ measurements. *Adv. Atmos. Sci.* **2017**, *34*, 559–570. [[CrossRef](#)]
29. Yuan, J.; Zhao, D.; Yang, R.; Yang, H. Predecessor rain events over China's low-latitude highlands associated with Bay of Bengal tropical cyclones. *Clim. Dyn.* **2018**, *50*, 825–843. [[CrossRef](#)]
30. Zhou, Y.; Guo, Y.; Yu, F. Analysis of a Rainstorm Process under the Joint Action of Westerly Trough and Typhoon in Sichuan Basin. *Plateau Mt. Meteorol. Res.* **2020**, *40*, 11–17. (In Chinese)

Disclaimer/Publisher's Note: The statements, opinions and data contained in all publications are solely those of the individual author(s) and contributor(s) and not of MDPI and/or the editor(s). MDPI and/or the editor(s) disclaim responsibility for any injury to people or property resulting from any ideas, methods, instructions or products referred to in the content.